

Exploiting Complementary Terahertz Ellipsometry Configurations to Probe the Hydration and Cellular Structure of Skin In Vivo

Xuequan Chen, Qiushuo Sun, Jiarui Wang, Hannah Lindley-Hatcher, and Emma Pickwell-MacPherson*

The noninvasive and water-sensitive characteristics of terahertz (THz) light make it highly attractive for in vivo studies, especially for skin applications. However, THz instrumentation has not been developed sufficiently to fully explore all the potential applications arising: current systems cannot obtain uncorrelated reflections from multiple configurations to determine the complicated structure of living tissues. Herein, this bottleneck is overcome by implementing a novel ellipsometry configuration able to efficiently provide four complementary sets of spectral ratios, significantly enhancing characterization capabilities. An accurate model of the skin is established and validated. The anisotropy of the stratum corneum (SC) caused by its cellular structure is verified both theoretically and experimentally. The in vivo response of skin on the volar forearm to occlusion is observed by the dynamic changes in the SC and the epidermis. In addition, the THz dispersion and birefringence sensitively probe the level of hydration and the cellular inhomogeneity, producing results in good agreement with microscope images and the biological processes of the SC. The presented technique offers a brand-new functionality in extracting insightful structural information from complex systems, significantly extending the versatility of THz spectroscopy.

1. Introduction

Terahertz (THz) waves are a promising tool for in vivo spectroscopy and imaging because they are nonionizing, noninvasive, and highly sensitive to water.^[1] In vivo THz measurements have demonstrated potential for diagnosing numerous conditions such as skin burns,^[2] skin cancer,^[3] scars,^[4] and diabetic foot syndrome.^[5] The focus of in vivo studies is largely on the skin due to the short penetration depth of THz light in biological tissues. Most of these studies were carried out using THz time-domain spectroscopy (THz-TDS), which has a wide range of applications due to its broad bandwidth and electric-field detection abilities.

To carry out measurements in vivo, a reflection measurement of the sample is usually compared with a reference measurement of a known medium, an optical model is then used to equate the ratio of these two measurements to physically relevant parameters for the skin. This methodology has not significantly progressed despite the rapid growth in the number of applications. An obvious bottleneck arises from limitations in the information that can be obtained: standard THz-TDS is not able to determine the complicated structure of skin, with its multiple layers, depth-dependent profiles and dynamic variations. Mathematically, only one set of frequency-dependent complex properties (e.g., the complex refractive index $\tilde{n}(\omega)$) can be uniquely characterized when only one spectral ratio is measured, such as by solving $f[\tilde{n}(\omega)] = \tilde{E}_{\text{sample}}(\omega) / \tilde{E}_{\text{reference}}(\omega)$, where $\tilde{E}_{\text{sample}}(\omega)$ and $\tilde{E}_{\text{reference}}(\omega)$ refer to the sample and reference signals in the frequency-domain.^[6] As a compromise, researchers have employed models to simplify the system and reduce the number of unknown parameters. A typical example is the stratified medium theory proposed by Bennett et al. that utilizes effective medium theory (EMT) to represent the frequency-dependent permittivity using a single water concentration value.^[7] Sun et al. further used this theory to derive a model for the swelling of the stratum corneum (SC) which can be used to analyze water diffusivity in occluded skin.^[8,9] However, these simplifications limit the information that can be extracted from the measurements and to some extent sacrifice the accuracy. Also, different simplifications yield inconsistent results in different studies.

Dr. X. Chen, J. Wang, Prof. E. Pickwell-MacPherson
Department of Electronic Engineering
The Chinese University of Hong Kong
Hong Kong 999077, China
E-mail: E.MacPherson@warwick.ac.uk

Dr. Q. Sun
Department of Physics and Astronomy
University of Birmingham
Birmingham B15 2TT, UK

H. Lindley-Hatcher, Prof. E. Pickwell-MacPherson
Physics Department
Warwick University
Coventry CV4 7AL, UK

 The ORCID identification number(s) for the author(s) of this article can be found under <https://doi.org/10.1002/adpr.202000024>.

© 2020 The Authors. Published by Wiley-VCH GmbH. This is an open access article under the terms of the Creative Commons Attribution License, which permits use, distribution and reproduction in any medium, provided the original work is properly cited.

DOI: 10.1002/adpr.202000024

For example, occlusion decreased the extinction coefficient of the skin in a single layer skin model,^[10] whereas the opposite result was found when the skin was modeled as a bilayer structure.^[11] Despite the great potential of THz spectroscopy for biomedical applications, the ability to accurately and credibly interpret the data is fundamental for future applications in clinical diagnosis.

In this work, we present a revolutionary technique to significantly enhance the characterization capabilities of THz spectroscopy. We have designed a multiconfiguration ellipsometer, which can be efficiently switched between four uncorrelated configurations to provide four sets of complex spectral ratios. These greatly enriched data enable us to develop and test a comprehensive model of the skin capable of approximating its complex structure, taking the anisotropy of the SC into consideration for the first time. The model was theoretically derived from the flattened cellular structure before being verified experimentally. Human skin measurements were taken of the volar forearm region to investigate the THz responses to occlusion. We show that the properties of the SC ordinary/extraordinary components and the epidermis, can be independently characterized without using EMT. The time variation of the frequency profiles clearly demonstrates the dynamic responses of the skin. More importantly, the abundant information enables the calculation of the dispersion and birefringence of the SC, making it possible to deduce the hydration and cellular structure of skin, yielding results which are consistent with the biological processes within the SC and microscope images.

2. Methods

2.1. Multiconfiguration THz Ellipsometer

The limited information obtained from a measurement fundamentally restricts the characterization capability. The solution is to measure a subject in multiple highly uncorrelated configurations, such as using different polarizations and incident angles. Ellipsometry is a good option in principle.^[12] Yet, traditional THz ellipsometers do not solve this problem because the polarization state E_p is compared with E_s , giving only one spectral ratio as no reference is taken.^[13] This is efficiently solved by introducing a prism or a window to obtain a reference without phase uncertainty, because good contact can usually be achieved

between skin and a reflection plane. Using this approach, two uncorrelated spectral ratios $E_{p\text{-sample}}/E_{p\text{-reference}}$ and $E_{s\text{-sample}}/E_{s\text{-reference}}$ can be obtained. In contrast, measuring reflections from multiple angles is more challenging. Varying the incident angle can be relatively simple in fiber-based systems.^[13] However, manually changing the angle introduces errors and misalignments with each adjustment. Also performing this change would take several minutes, which would be too long for in vivo measurements because biological parameters are mostly time varying. For example, investigation of skin occlusion shows a peak-to-peak variation of 6%, 3%, and 2% in the first, second, and third minutes, respectively.^[10] Moreover, the angle selection is critical to ensure the low correlation of the different configurations. It is required that the angles should be sufficiently different while at the same time be sensitive to the polarization. These requirements can be better understood by considering cases where they are not satisfied. For example, the reflections from two similar incident angles provide nearly the same information, or the p - and s -reflections will be almost identical at near normal incidence.

To overcome these difficulties, we introduced the double prism system shown in **Figure 1a**. The region of interest is placed on top of the upper right-angle silicon (Si) prism (with a removable Si wafer connected). Another right-angle prism with gold-coated surfaces is symmetrically mounted under the Si prism acting as a perfect mirror. Placing the double-prism system in transmission makes it possible to establish two different optical paths by changing the height. The beam can either be directly refracted into the upper Si prism, or be reflected by the lower prism first to alter the entry angle at the Si prism by 90° . The incident angles to the Si-subject (or air) interface in both cases are denoted as θ_{i1} and θ_{i2} , which are determined to be 56.94° and 33.06° , respectively using $n = 3.418$.^[14] The 90° difference in the entry angle to the Si prism provides distinct reflections from the two beams. This ensures the reflections from the two angles have very low correlation. Furthermore, the use of a Si prism plays a key role in providing extremely high sample-sensitivity and polarization-dependence,^[15] which is enabled by its significantly larger refractive index (≈ 3.4) compared with biotissues (usually around 2). This greatly reduces the correlation between the p - and s -polarized reflections.

The double-prism system is fixed on a motorized linear stage (SIGMAKOKI Shot-602) to precisely control the vertical position,

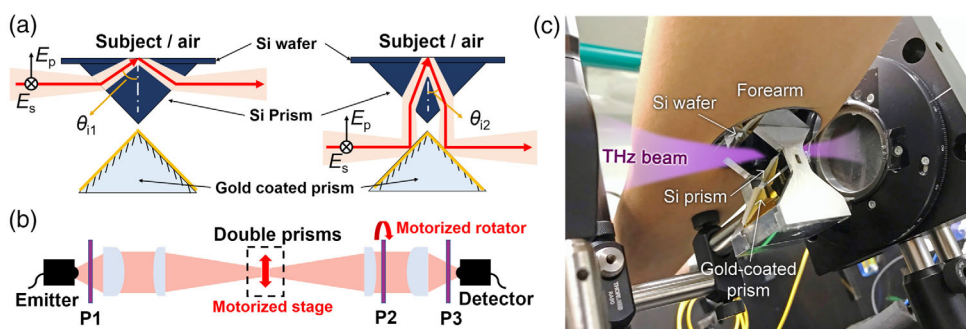


Figure 1. Schematic of the system and illustration of the skin measurement. a) Schematic of the double-prism system and the two alternative optical paths. The double-prism system is mounted on a motorized stage assembly in b) a transmission-form ellipsometer. Switching the incident angle and the polarization enables four uncorrelated configurations. c) Labeled photo showing a skin measurement being taken on the double-prism system.

as shown in the dashed rectangle in Figure 1b. Three polarizers were used, indicated by P1, P2 and P3. P1 and P3 were both fixed at 45° (to *p*- or *s*- direction), whereas P2 was mounted on a motorized rotator to select the *s*- or *p*-reflections. Technical details of the THz optics can be found in our ellipsometry paper.^[13] The focusing lenses have a large f-number of 2.8, which reduces the divergence of the incident angle and its influence on the characterization.^[13] The polarizations and incident angles can be efficiently and precisely controlled by the motorized rotator and stage to provide four uncorrelated configurations. In detail, *p*- and *s*- Si-skin reflections are successively obtained in 20 s at an incident angle of θ_{i1} by rotating P2 (which takes 3 s). The linear stage then lifts the double-prism system up by 1.6 cm (in 5 s) and changes the incident angle to θ_{i2} , where another set of *p*- and *s*- reflections are measured. After that, the stage lifts the double-prism system up again by 2.5 cm to exit the beam region (with the skin still keeping in contact with the Si), allowing a transmission signal to be directly measured. If a subject is to be measured continuously, the stage then moves back to θ_{i1} and the skin measurements are repeated. After completing all subject measurements, four Si-air reflections from the four configurations were measured as the references. The transmission signal was also recorded after the reference measurements. These transmission signals record the signal variations during the measurement. By comparing each of them to the last one measured after the reference signals, we can calibrate the skin reflections for the power variation and pulse shift induced by any disturbance, including the humidity changes. This enables the Si-air references to be quickly taken after all subject measurements such that the skin can keep in contact with the Si for the duration of the study. A photo taken during a skin measurement of the volar forearm is shown in Figure 1c. The space around the double-prism system is empty, allowing the forearm (or other investigated regions) to be easily and stably kept in place. The Si wafer can slightly embed into the soft skin to provide good contact. The subjects measured were seated and able to rest their arm comfortably, so as to keep the area being measured in place for the duration of the measurements. The automatic program control of the rotator and stage enables a robust, accurate and fast (5 s) change between the four configurations. The four sets of uncorrelated reflections notably enrich the information and enhance the characterization capabilities, enabling an accurate skin model to be established and characterized.

2.2. Anisotropic SC Skin Model

Models of the skin describe the light-skin interaction to relate the obtained THz signals to physical skin parameters. Regarding the skin as a homogeneous medium over-simplifies the skin structure as the SC-epidermis reflection is not considered.^[4,10,16] Separating the SC from the epidermis is a better approximation of the real structure,^[17] but it introduces two sets of unknown parameters (for the SC and epidermis). To further consider the water gradient revealed by Raman spectroscopy,^[18,19] Bennett et al. proposed a stratified medium theory to account for the water distribution.^[7] As the model complexity increases, additional simplifying theories are needed. The most important one is the two-component EMT, which decomposes biological

tissues into a biological background (i.e., the properties of the dehydrated tissue, assumed to be known a priori) and a water component. However, there are problems with using this model, first the properties of the biological background are uncertain and are usually approximated using dehydrated porcine skin, in addition, a two-component EMT is not strictly valid. Many studies have shown that hydrated water (also called bound water), which refers to the water hydrogen-bonded to other molecules, has different THz properties from those of free water.^[20,21] Extensive studies of the interaction of water with sugars,^[22] proteins,^[23] and phospholipids,^[24] conclude that an EMT with at least three components should be used to account for the properties of hydrated water. This is also applicable to skin as most water molecules exist in a bound form in the skin.^[25] More importantly, the flattened SC cellular structure introduces anisotropy that has never been explored previously, which also invalidates EMT assumptions.

The SC is a two-compartment structure formed by flattened corneocytes (the SC cells) surrounded by a lipid matrix, commonly referred to as the “brick and mortar” structure.^[26] Corneocytes are about 1 μm thick and 30 μm in diameter,^[27] stacking to form 15–20 layers in the forearm region, as shown in Figure 2a. Water is mostly preserved in the corneocytes by binding to the natural moisturizing factors (NMFs), with very little present in the lipids,^[28,29] this means that water is in a bound form in the SC. The lipids are also in a lamellar arrangement,^[30] acting as barriers to prevent dehydration.^[27] The inhomogeneous water distribution results in a significantly larger complex refractive index \tilde{n} in the corneocytes compared with the surrounding lipids.^[31] From the cross-sectional view shown in the left part of Figure 2b, this difference in properties can be modeled as a periodic alternation of \tilde{n} in the vertical direction, forming a two-component lamellar layered structure. When the layer thickness is significantly smaller than the wavelength, such SC structure can be modeled as an uniaxial anisotropic medium, with its ordinary and extraordinary complex refractive indices (\tilde{n}_{SC-o} and \tilde{n}_{SC-e}) being effectively related to the complex refractive indices of the corneocyte (\tilde{n}_{corn}) and lipid (\tilde{n}_{lip}) as^[32,33]

$$\tilde{n}_{SC-o}^2 = f_1 \tilde{n}_{corn}^2 + f_2 \tilde{n}_{lip}^2 \quad (1)$$

$$\tilde{n}_{SC-e}^2 = \frac{1}{f_1/\tilde{n}_{corn}^2 + f_2/\tilde{n}_{lip}^2} \quad (2)$$

where f_1 and f_2 are the volume fractions of the corneocyte and lipid, respectively. The directions of the ordinary and extraordinary components are shown in Figure 2b. To verify the presence of birefringence in the SC, we calculated the reflections from the four systematic configurations using the layered SC structure and the corresponding effective anisotropic structure. In detail, we assign $\tilde{n}_{lip} = 1.5 - 0.1i$ and $\tilde{n}_{corn} = LLL(1.8 - 0.2i, 60\% \tilde{n}_{water})$, respectively, where LLL is the Landau, Lifshitz, Looyenga EMT to calculate \tilde{n}_{corn} using a biological background ($\tilde{n}_{bio} = 1.8 - 0.2i$) and a 60% volume fraction of water.^[34] Similarly, the complex refractive index of the epidermis \tilde{n}_{Ep} is given by $LLL(1.8 - 0.2i, 75\% \tilde{n}_{water})$.^[7] \tilde{n}_{water} , \tilde{n}_{lip} , \tilde{n}_{corn} , and \tilde{n}_{Ep} are shown in Figure 2c,d. Notice that the LLL EMT is used only to assigned values for the theoretical verification, without being applied in the experimental characterization.

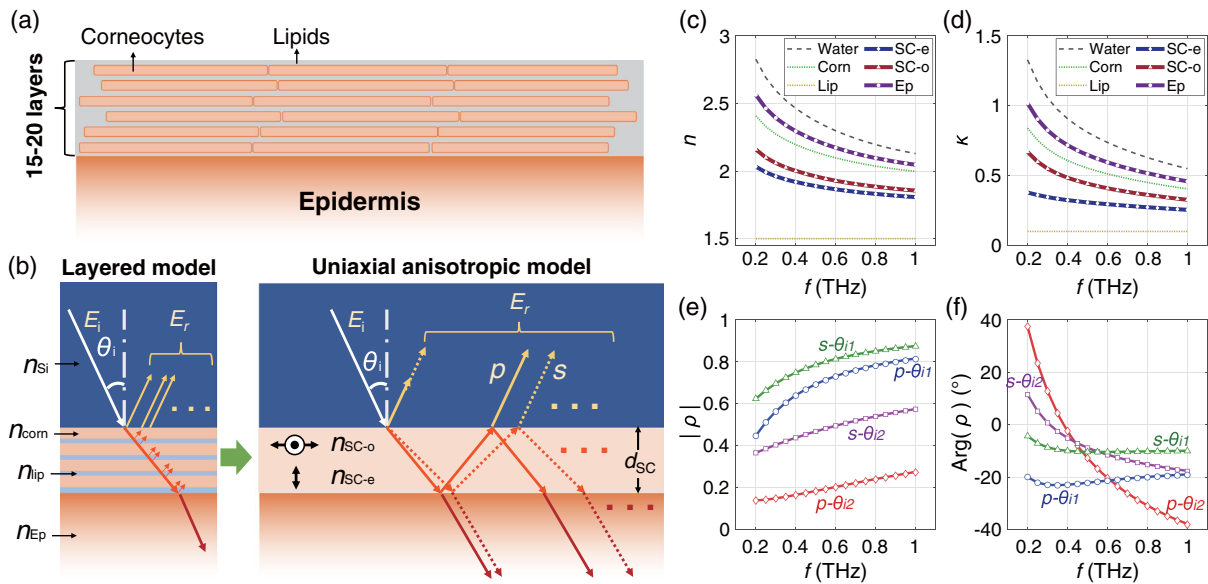


Figure 2. Skin structure and the theoretical verification of the anisotropic SC. a) Cellular structure of the skin and b) its corresponding optical layered model (left) and the equivalent anisotropic model (right). c) Refractive index n and d) extinction coefficient κ of water, corneocyte, lipid, and epidermis assigned in the calculation of the layered model, and the effective SC-e and SC-o components calculated using Equation (1) and (2). e) Magnitude and f) phase of the theoretical reflection ratios ρ . The symbols are the results from the layered model and the solid curves are the results from the anisotropic model. The labels near the curves indicate the corresponding configurations used for the calculations.

The lipid and the corneocyte thicknesses are assigned as 0.4 and 0.9 μm , respectively. They are periodically stacked for 15 layers, resulting in a total SC thickness of $d_{\text{SC}} = 19.5 \mu\text{m}$. With these assigned values, we calculated $\tilde{n}_{\text{SC-o}}$ and $\tilde{n}_{\text{SC-e}}$ using Equation (1) and (2), which are shown in Figure 2c,d. The reflections from the layered SC structure can be calculated using the multiple-layer Fresnel equations,^[12] with the reflection ratios $\rho = \tilde{E}_{\text{Si-skin}}(\omega)/\tilde{E}_{\text{Si-air}}(\omega)$ in the four experimental configurations shown as the symbols in Figure 2e,f. The reflection ratios from the anisotropic SC structure are shown as the solid curves in Figure 2e,f (see Supporting Information Section 1).^[12] A perfect match can be found for all the four ratios between the two models, strongly proving that the lamellar layered structure can be physically modeled by the anisotropic structure. Instead of using the layered model in our later experimental characterization, we used the anisotropic model to avoid needing to know the corneocyte/lipid thickness and the influence of the imperfect layered structure in a real SC. In addition, we can explore the level of inhomogeneity of the cellular structure from the birefringence. For example, if the SC is highly homogeneous, such as if \tilde{n}_{lip} is close to \tilde{n}_{corn} or f_1 is nearly 1, Equation (1) and (2) result in $\tilde{n}_{\text{SC-o}}$ and $\tilde{n}_{\text{SC-e}}$ being identical (i.e., zero birefringence).

2.3. Characterization Method

Our characterization numerically optimizes $\tilde{n}_{\text{SC-o}}(\omega)$, $\tilde{n}_{\text{SC-e}}(\omega)$ and $\tilde{n}_{\text{ep}}(\omega)$ by fitting the theoretical ratios to the experimental results. The SC thickness d_{SC} is an unknown parameter, and theoretically it can also be determined from the fitting. However, the fit is found to have limited sensitivity to d_{SC} which gives the determined thickness a lower accuracy compared with

the reference value measured by confocal Raman spectroscopy.^[19] Therefore, we used a reference thickness of $d_{\text{SC}} = 20 \mu\text{m}$ in all measurements. The thickness uncertainty analysis is detailed in the Supporting Information Section 2, which concludes that there is little influence on the experimental results and corresponding conclusions.

$\tilde{n}_{\text{SC-o}}(\omega)$, $\tilde{n}_{\text{SC-e}}(\omega)$, and $\tilde{n}_i(\omega)$ contain a large number of data points causing classical iteration methods difficulty to converge. A heuristic algorithm can be used to improve the convergence and reduce the computational complexity. In this work, we adopted a genetic algorithm (GA) for the optimization. GAs mimic the natural evolution process, and search for the optimized solution from a set of random initial solutions. Compared with traditional iteration methods that start from a single solution, GAs are not sensitive to the initial values of the parameters and can robustly approach the global minimums in a large searching space. It has been successfully applied in model fitting,^[35] THz adaptive sampling,^[36] and THz denoising.^[37] To further improve the optimization accuracy, we use a proper function to initialize $n(\omega)$ and $\kappa(\omega)$ to further reduce the searching space. This can be done using an offset exponential function to set $n(\omega)$ or $\kappa(\omega) = ae^{b\omega} + c$. As shown in our recent work, it can precisely describe material properties ranging from transparent to absorptive samples.^[6] In this way, the number of unknown parameters in the frequency domain is reduced to three (i.e., a , b , and c). During the measurement, the Si prism is found to warm up from making contact with the skin, this changes the Si refractive index and shifts the THz pulses for an unknown range.^[38] The pulse shift $\Delta\tau$ is also considered an unknown parameter to be determined in the optimization to calibrate the phase errors. This algorithm is detailed in Supporting Information Section 3.

3. Experiments

3.1. Measurement Protocol

The study was approved by the Joint CUHK-NTEC Clinical Research Ethics Committee and written informed consent was obtained from all volunteers to partake in the study. The skin on the volar forearm of five subjects, age 25–29, with three males and two females, was measured. The forearm was placed on the Si prism and measured by the proposed ellipsometer for 30 min at 2 min intervals (starting from 1 min to avoid the rapid occlusion effect at the very beginning), providing 16 groups of data (each group containing four reflections). Each reflection was recorded once using a slow scan mode, which takes about 10 s to obtain a good signal-to-noise ratio. The forearm was kept in contact with the Si prism during the measurement without being moved. The Si-air references in the corresponding four

Table 1. Experimental protocol.

	1. Place the forearm on the Si for 1 min.
Repeat for every 2 min for 16 times	2. <i>p</i> - and <i>s</i> - Si-skin reflections measured at θ_{11} .
	3. Stage moves up by 1.6 cm and change to θ_{12} .
	4. <i>p</i> - and <i>s</i> - Si-skin reflections measured at θ_{21} .
	5. Stage moves up by 2.5 cm. The prisms are removed from the beam region with the skin keeping in contact with the Si.
	6. Transmission signal measured.
	7. <i>p</i> - and <i>s</i> - Si-air references measured at θ_{11} and θ_{21} . Transmission signal measured.

configurations were only measured after all the skin measurements had been completed. **Table 1** shows the measurement protocol. All the measurements were conducted without dry air purging because the studied frequency range of 0.2–1 THz has high signal-to-noise ratios and low water-vapor absorptions. The requirement on changing the optics during the measurement would also introduce difficulties in achieving a full-purging environment. However, any signal fluctuations caused by humidity variation will be compensated for using the transmission signal measured after every group of skin measurements.

3.2. Experimental Verification

We show the experimental results of subject 1 as an example to verify the proposed ellipsometer and the skin model. The discrete data in **Figure 3a,b** show the magnitude and phase of the spectral ratios ρ measured at 31 min (i.e., occluded skin) using the configurations indicated by the labels near the data. The error bars were calculated from the noise level of the reflected signal, they are considerably small due to the good signal-to-noise ratio in the studied frequency range. The corresponding solid curves of similar colors are the best fits from the characterization. Both the magnitude and phase fit well with the model, showing convergent optimization. The curves are separated and non-linearly correlated, indicating the distinct reflection coefficients of different configurations to provide highly uncorrelated information. **Figure 3c,d** shows the real and imaginary parts of $\tilde{n}_{SC-e}(\omega)$, $\tilde{n}_{SC-o}(\omega)$ and $\tilde{n}_{Ep}(\omega)$ extracted from the best fit. They are independently characterized from the fitting without using an EMT to restrict their frequency profiles. Both $\tilde{n}_{SC-o}(\omega)$ and $\tilde{n}_{SC-e}(\omega)$ are lower than $\tilde{n}_{Ep}(\omega)$, while all of them are below $\tilde{n}_{water}(\omega)$ at 30 °C. The results in **Figure 3a–d** also have values close to those which

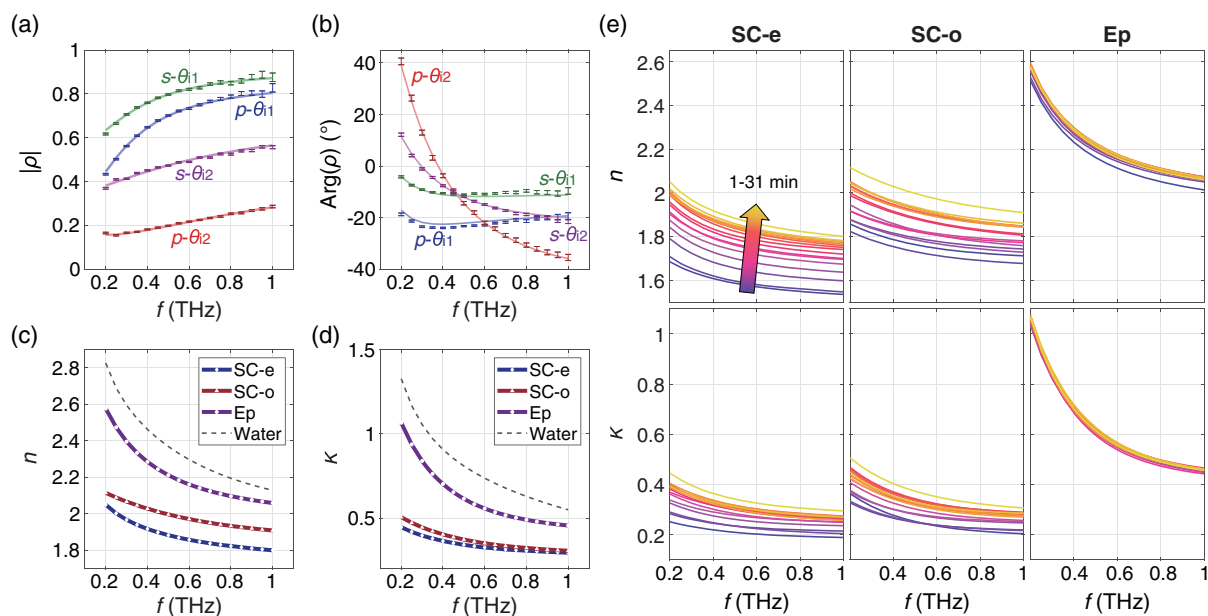


Figure 3. Experimental verification of the skin model and the system. a) Magnitude and b) phase of ρ from the experimental results (discrete data with error bars) and the best fit by the characterization (solid curves) under the four configurations indicated by the labels nearby. c) n and d) κ of the three extracted skin components, compared to that of water at 30 °C. e) n and κ of SC-e, SC-o, and Ep (epidermis) in the frequency domain. Curves with colors from blue to yellow are the results from 1 to 31 min, as indicated by the arrow.

have been theoretically verified in Figure 2c–f. These reflect the reasonable water concentrations for the SC and epidermis.^[7,11] Their relative positions clearly demonstrate the SC-epidermis structure and their distinct biological properties. Most importantly, the birefringence is clearly observed, and $\tilde{n}_{SC-e}(\omega)$ is found to be smaller than $\tilde{n}_{SC-o}(\omega)$ in line with the results from the theoretical calculation and the literature.^[33,39] This experimentally verifies the existence of THz birefringence in the lamellar SC cellular structure.

n and κ of subject 1 measured in the 30 min period are shown in Figure 3e as a function of frequency. Colors from blue to yellow are the results from 1 to 31 min, as indicated by the arrow, showing the dynamic changes in the skin due to occlusion. Both $\tilde{n}_{SC-o}(\omega)$ and $\tilde{n}_{SC-e}(\omega)$ increase with the measurement time in the studied frequency range, whereas $\tilde{n}_{Ep}(\omega)$ is nearly constant. This clearly verifies the proposed occlusion mechanism that water molecules aggregate in the SC when evaporation is prevented due to occlusion, while the water concentration remains unchanged in the epidermis. Progressing from the previous work that either shows only the amplitude change,^[40] or simplifies the skin as a homogeneous medium,^[10] the independently extracted SC and epidermis properties clearly demonstrate the occlusion process and the variation in each layer. Although the relative positions of the three skin components are reasonable in terms of their water concentration, one may also notice the relatively low values of n_{SC-e} in the first few minutes. At high frequencies, n_{SC-e} can be close to 1.5, which is unrealistic as even the lipids in the SC should have $n > 1.5$.^[31] This can be explained by the contribution of air due to a rough skin surface and

disorganized lipid structure, and is explained in more detail in Section 3.4.

3.3. Skin Dynamics during Occlusion

The skin dynamics can be seen from the time dependence of n and κ . We select the middle frequency of 0.6 THz to plot Figure 4 as different frequencies show similar variation profiles in Figure 3e. n and κ of the five subjects are shown in Figure 4a,b, respectively. The first obvious characteristic is the increasing n and κ with time of the two SC orientations, whereas the epidermis is nearly unchanged. The highly consistent characteristic for the five subjects further confirms the occlusion dynamics discussed earlier. The occlusion rate is faster at the beginning and becomes slower with time, but the skin was not fully saturated even after 30 min. These observations are also consistent with our previous studies.^[10] For all subjects, $\tilde{n}_{SC-o}(\omega)$ is found to be higher than $\tilde{n}_{SC-e}(\omega)$, consistent with the anisotropic theory. In addition, we note that $\tilde{n}_{SC-o}(\omega)$ is noisier than $\tilde{n}_{SC-e}(\omega)$, which is caused by the better sensitivity of the configurations to the SC-e component (see Supporting Information Section 4).

3.4. Hydration and Structural Profiles

3.4.1. Dispersion and Birefringence

n and κ are usually understood to represent the hydration level because water dominates their values in biological samples.

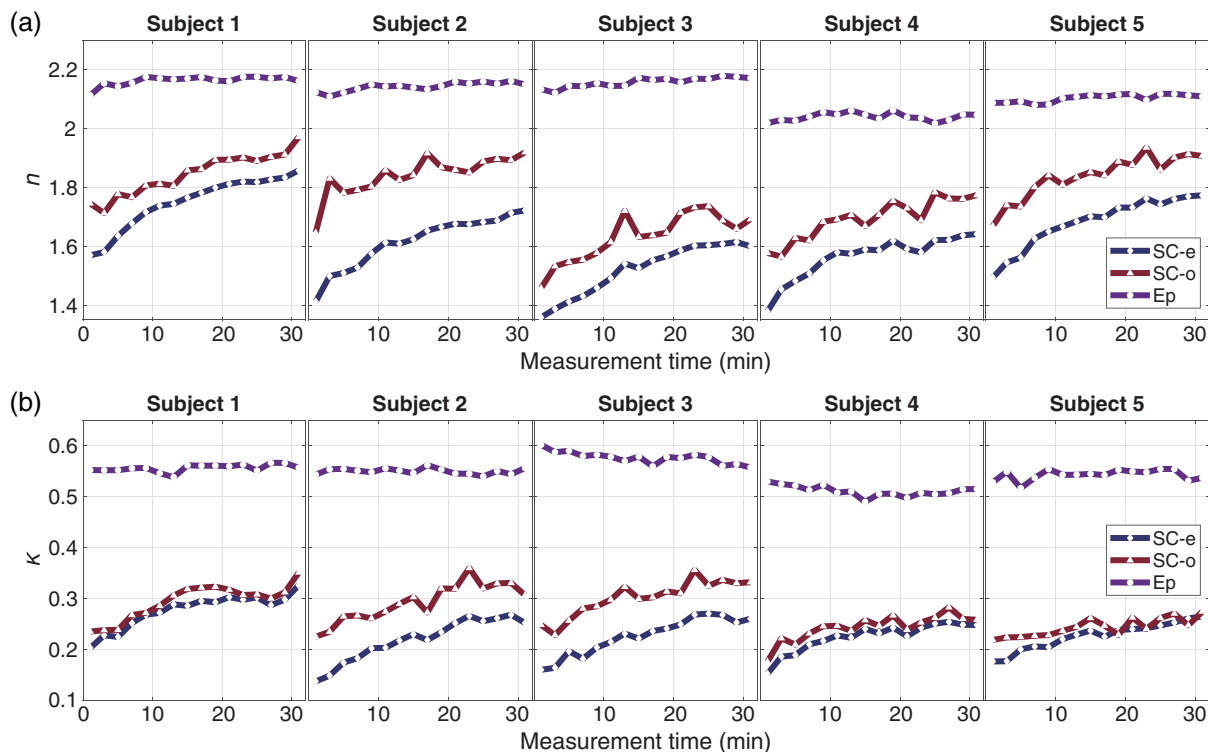


Figure 4. THz dynamic properties during skin occlusion. a) Experimental n and b) κ at 0.6 THz of the SC and epidermis as a function of measurement time for the five subjects.

However, in the anisotropic skin model, both the water concentration and the cellular structure affect n and κ values, which is reflected by the different relative positions of SC-e and SC-o components for different subjects in Figure 4. Herein, we use dispersion and birefringence to independently explore the hydration and structural properties.

Dehydrated tissues are approximately achromatic,^[31] whereas water is highly dispersive due to molecular relaxations.^[38] The dispersion of a water-hydrated biological tissue is positively correlated to its water concentration and is less relevant to the cellular structure. As both n and κ monotonically decrease with frequency in water, the dispersion can be represented by the difference between the first and the last frequency points:

$$\text{Dispersion} = |\tilde{n}_{\text{SC-e}}(\omega_1) - \tilde{n}_{\text{SC-e}}(\omega_m)| \quad (3)$$

where ω_1 and ω_m are the angular frequencies at 0.2 and 1.0 THz, and m denotes the index. We used only the SC-e component due to the smaller error. On the other hand, the birefringence reflects the inhomogeneity of the SC. We calculate the birefringence of n and κ using Equation (4) and (5), respectively.

$$n\text{Bir} = \sum_{\omega_1}^{\omega_m} [n_{\text{SC-o}}(\omega) - n_{\text{SC-e}}(\omega)]/m \quad (4)$$

$$\kappa\text{Bir} = \sum_{\omega_1}^{\omega_m} [\kappa_{\text{SC-o}}(\omega) - \kappa_{\text{SC-e}}(\omega)]/m \quad (5)$$

The dispersion and birefringence of the five subjects are shown as the symbols in Figure 5. To better show the long-term time-variation, the solid curves smooth the raw data by calculating the moving average based on the central value and two points either side where possible. The values of the curves at 3 and 29 min are the average of three data points (1,3,5 and 27,29, and 31) and the values at 1 and 31 min are equal to the raw data. The first obvious characteristic is the remarkably increased dispersion with time, directly showing the increasing hydration level due to occlusion. The dispersion values are almost all doubled in 30 min for all subjects, showing a consistent occlusion effect. The dispersions have similar profiles to $\tilde{n}_{\text{SC-e}}$, but they are not exactly proportional to each other. For example, subjects 3 and 4 have similar $\tilde{n}_{\text{SC-e}}$ in the last 10 min, whereas the corresponding dispersion values of subject 3 are higher. This verifies that the cellular structure also affects the complex refractive index, which can be observed from the birefringence.

The birefringence results in Figure 5 are noisier than that of the dispersion because the noisier SC-o component is used. However, we can still observe the overall variation trend from the averaged curves. For $n\text{Bir}$, the results from all subjects decrease with time. This indicates the level of inhomogeneity in the SC was changed by the occlusion. For κBir , the time

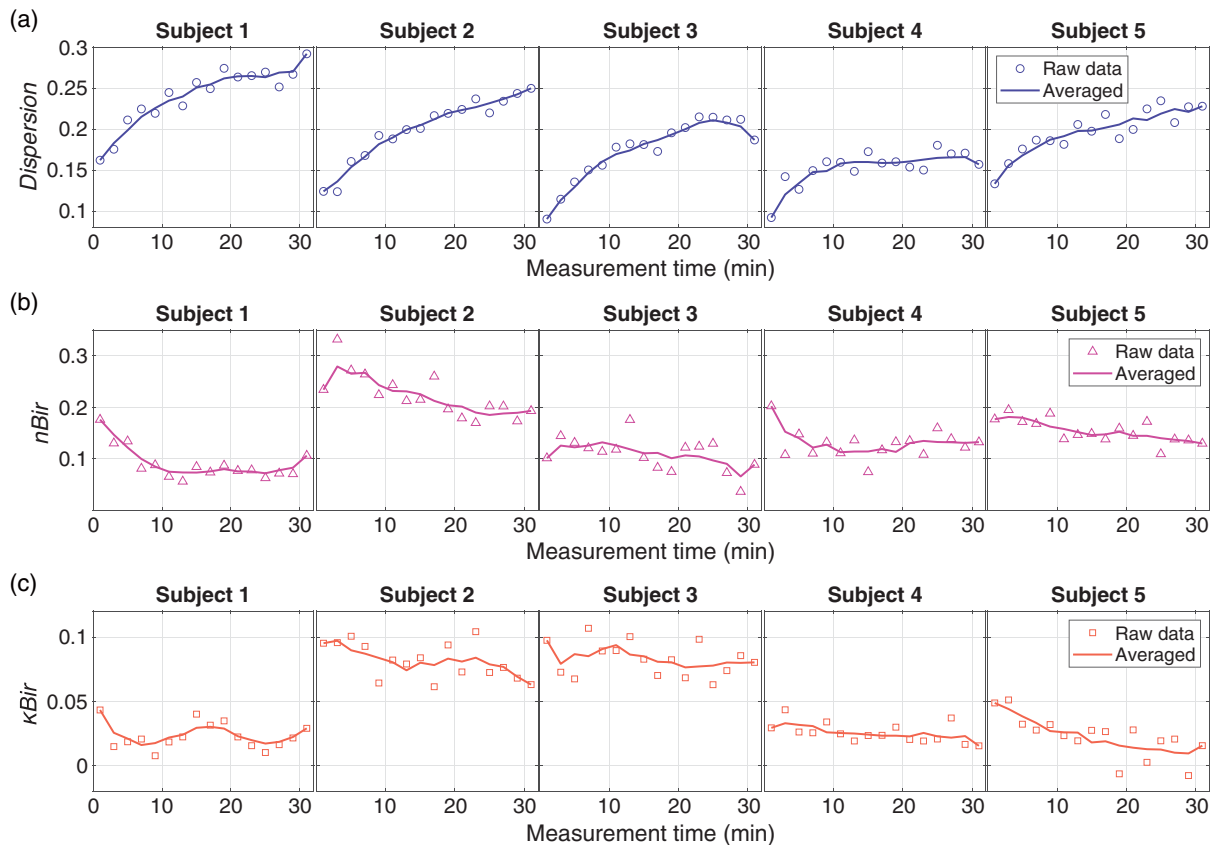


Figure 5. Dispersion and birefringence of skin during occlusion. a) Dispersion, b) $n\text{Bir}$, and c) κBir of the five subjects as a function of measurement time.

variation is less obvious. Only weak decreasing profiles can be observed for subjects 2 and 5. This can be interpreted by the following analysis on the occlusion-induced structural changes in the SC.

3.4.2. Biological Cellular Structure

To better explore the biological structural variations, we imaged the skin in the same experimental conditions using a $5\times$ visible microscope. In detail, the forearm skin of subject 2 was kept in contact with a transparent sapphire window for 30 min to simulate the THz measurement conditions and images of the skin were acquired every 5 min. The results are shown in **Figure 6**.

Each circular imaging area is 7 mm in diameter, which is a similar size to the focused THz spot. The scale bars are 1 mm. The skin continues to become increasingly smooth throughout occlusion. The furrows (dark lines) and the scattered light (bright areas) fade, which can be clearly seen up to 20 min. The rough features can potentially scatter the THz light that may introduce errors in the characterization. We have conducted numerical simulations in Supporting Information Section 5 to prove that the THz scattering is negligible in the configurations used. We zoom in on the images at 0 and 30 min at the bottom of **Figure 7** to better compare the occlusion effect, labeled as 1 and 2, respectively. The scale bars are $500\ \mu\text{m}$. Above the images, we have plotted the layered cellular structure in a cross-section view according to the images and the biological response of skin to occlusion. At the top of **Figure 7**, we show the depth profile of n and κ according to the cellular structure to investigate their inhomogeneities.

Image 1 shows the original state of the skin. It consists of obvious furrows separating the surface into randomly orientated triangular areas. These raised triangular areas are rough, shown by the scattering of white light. The rough surface makes poor contact with the Si,^[18] as shown in the cross-sectional view. Inside the SC there are stacked corneocytes and lipid lamellae, which are known to be depth dependent. Toward the SC outer surface, there is a reduced lipid density, disrupted lipid lamellar structure, and weaker corneocyte cohesion.^[41–43] The corneocytes are loosely connected by fewer, more disorganized lipids near the SC surface. As a result, the n distribution is analogous to a square wave but increases with depth. The lower lines represent the effective n_{lip} , whereas the upper lines are the effective n_{corn} . They both increase with depth due to the smaller air composition with the reduced furrows, roughness and disorganized lipids, and they finally approach the normal values of n_{lip} and n_{corn} toward deeper SC, indicated by the dashed lines. The increased effective n_{corn} also represents an increasing water

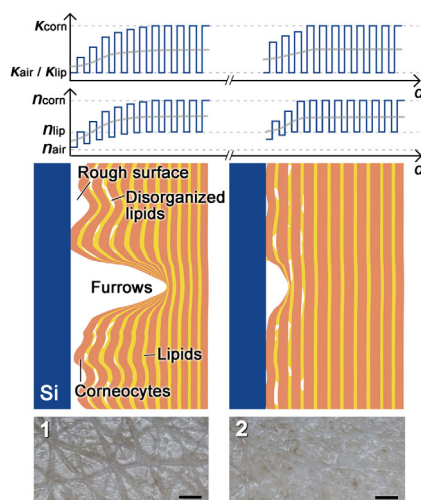


Figure 7. Illustration of the n and κ depth-profiles (upper) according to the cross-sectional SC structures (middle) and the microscope images (bottom) when the skin is nonoccluded (labeled 1) and occluded for 30 min (labeled 2). The scale bars are $500\ \mu\text{m}$. The cross-sectional structures were plotted according to the biological response of skin and the microscope images.

concentration with depth, consistent with that revealed by confocal Raman spectroscopy.^[18,44] The air components reduce the overall effective refractive index of the SC, this explains the low $n_{\text{SC}-e}$ values in the first few minutes in **Figure 3e**. The κ distribution is slightly different from that of n . The effective κ_{corn} has the same profile as that of n_{corn} as they are both affected by the air composition. However, the effective κ_{lip} is nearly depth-independent because lipids have such a negligible absorption that mixing with air does not reduce their effective values.^[31]

After 30 min occlusion, image 2 shows an obvious change as both the furrows and the roughness become very faded. The cross section depicts the internal variation. The corneocytes swell in the depth direction to be in a more regular lamellar arrangement, occupying the air regions previously induced by the furrows and the roughness.^[45] The peripheral lipids remain disorganized as the water from occlusion stays predominantly in the corneocytes without affecting the lipid structure, while they are pushed forward toward the surface of the skin due to the swelling. The occlusion results in higher effective n_{lip} , n_{corn} , and κ_{corn} at the peripheral SC. The increased n_{corn} compared with the nonoccluded state gives a higher hydration level, agreeing well with the *Dispersion* results. The n and κ inhomogeneity can be evaluated from two aspects: the intercellular inhomogeneity and the depth inhomogeneity. The former

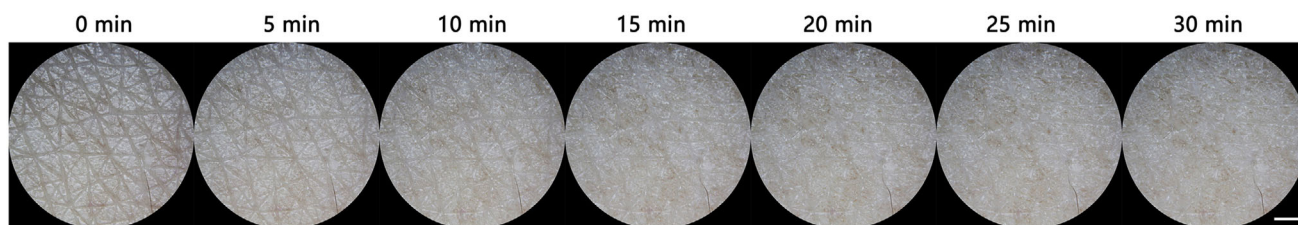


Figure 6. The microscope images of skin during occlusion, imaged from 0 to 30 min at 5 min intervals. The scale bar is 1 mm.

measures the effective n or κ difference between the corneocytes and the lipids. The latter evaluates the average n or κ variation across the SC depth, which is represented by the gray curves. They both contribute to the birefringence because they are both subwavelength. For n , as the occlusion increases both n_{ip} and n_{corn} , the intercellular inhomogeneity is not significantly changed, whereas the depth inhomogeneity must decrease as the average n changes less with depth, represented by the flattened gray curve. The total inhomogeneity of n is thus reduced, agreeing well with the decreased $nBir$ in Figure 5. For κ , the increased κ_{corn} enlarges the intercellular inhomogeneity but reduces the depth inhomogeneity. The κBir in Figure 5 shows very little variation with time due to these opposite changes balancing out.

The good agreement between the biological process and the THz properties demonstrates that THz spectroscopy is capable of being used to explore both the hydration and cellular structure of skin. In summary, dispersion isolates the influence of cellular structure to independently represent the hydration level. $nBir$ is found to be sensitive to the lamellar structure. A low $nBir$ usually represents a regularly organized lipid structure with few air components, which usually leads to a smooth skin surface. On the contrary, a large $nBir$ is induced by more air-components in the SC, either because of a rough skin surface or disordered lipids. These characteristics are highly related to the barrier function and the condition of the skin.^[46] Therefore, THz birefringence provides important and valuable information to evaluate the skin insightfully and noninvasively. The proposed technique significantly improves the functionality of THz spectroscopy to comprehensively characterize various aspects of the skin.

4. Conclusions

In this work, we present an insightful in vivo investigation of skin with THz spectroscopy, by using a revolutionary multiconfiguration ellipsometer. Four sets of uncorrelated spectral relationships were accurately achieved by efficiently switching in-between four measurement configurations, which strongly enhance the characterization capability. The enriched information allows an accurate skin model to be established, comprehensively considering the SC anisotropy originating from the layered cellular structure, which was derived theoretically and verified experimentally. The volar forearms of volunteers were measured, with the properties of the SC ordinary/extraordinary components and the epidermis being independently extracted using a GA-based characterization algorithm. The time variation of the frequency-domain profiles intuitively demonstrates the occlusion dynamics and the biological response of the skin to occlusion. Further analysis of the THz dispersion and birefringence insightfully reveals the hydration level and cellular structure variations, which are in good agreement with the biological studies and microscope images taken under the same experimental conditions.

The ability to robustly obtain uncorrelated spectra from multiple configurations is a great breakthrough in overcoming the bottleneck facing current THz techniques. Such an ability is extremely favorable as it enables more properties to be characterized, calibrates systematic errors (such as the pulse shift errors calibrated in this work), and reduces the experimental errors by fitting to more spectral ratios. In this work, the

uncorrelated spectra make it possible to validate an accurate skin model without over-simplifications. The anisotropic SC skin model was proposed for the first time, which calibrates the previous double-layer model by considering the birefringence from the flattened cellular structure. Such a complicated model is unsolvable using the single reflection measurement obtained using one configuration. Solving it by taking measurements with four uncorrelated configurations extracts comprehensive and insightful skin properties, making THz waves not only a water-sensitive tool but also capable of monitoring the cellular structure. Hydration level is only one aspect of the properties of the skin, which is also measurable using other techniques such as confocal Raman spectroscopy and corneometry. Monitoring the SC cellular structure has never been achieved so non-invasively and efficiently before, despite being important information necessary for skin evaluation. The observations of the cellular interactions between the SC and different substances move THz spectroscopy forward to be capable of in-depth clinical diagnosis, which is in high demand for analyzing numerous skin diseases, skin-related symptoms, or testing skin products and drugs. Future studies may further combine the results with other skin investigation tools to better interpret the data, building more relationships between the THz responses and biological properties. Apart from biological applications, this notably enhanced characterization capability is also very useful for materials with complicated structures or anisotropy, showing its great potential to serve as a platform to extend the versatility of THz spectroscopy into more research areas.

Supporting Information

Supporting Information is available from the Wiley Online Library or from the author.

Acknowledgements

This work was funded by the Research Grants Council of Hong Kong (14206717); Engineering and Physical Sciences Research Council (EPSRC) (EP/S021442/1); and the Royal Society Wolfson Merit Award.

Conflict of Interest

The authors declare no conflict of interest.

Keywords

anisotropy, cellular structures, hydration, in vivo, skin, terahertz ellipsometry

Received: July 30, 2020
Revised: October 26, 2020
Published online:

- [1] Q. Sun, Y. He, K. Liu, S. Fan, E. P. J. Parrott, E. Pickwell-MacPherson, *Quant. Imaging Med. Surg.* **2017**, *7*, 345.
- [2] M. H. Arbab, D. P. Winebrenner, T. C. Dickey, A. Chen, M. B. Klein, P. D. Mourad, *J. Biomed. Opt.* **2013**, *18*, 077004.

- [3] R. M. Woodward, B. E. Cole, V. P. Wallace, R. J. Pye, D. D. Arnone, E. H. Linfield, M. Pepper, *Phys. Med. Biol. To* **2002**, *47*, 3853.
- [4] S. Fan, B. S. Y. Ung, E. P. J. Parrott, V. P. Wallace, E. Pickwell-MacPherson, *J. Biophotonics* **2016**, *10*, 1143.
- [5] G. G. Hernandez-Cardoso, S. C. Rojas-Landeros, M. Alfaro-Gomez, A. I. Hernandez-Serrano, I. Salas-Gutierrez, E. Lemus-Bedolla, A. R. Castillo-Guzman, H. L. Lopez-Lemus, E. Castro-Camus, *Sci. Rep.* **2017**, *7*, 1.
- [6] X. Chen, E. Pickwell-MacPherson, *Sensors* **2019**, *19*, 4118.
- [7] D. B. Bennett, W. Li, Z. D. Taylor, W. S. Grundfest, E. R. Brown, *IEEE Sens. J.* **2010**, *11*, 1253.
- [8] Q. Sun, R. I. Stantchev, J. Wang, E. P. J. Parrott, A. Cottenden, T. W. Chiu, A. T. Ahuja, E. Pickwell-MacPherson, *J. Biophotonics* **2019**, *12*, e201800145.
- [9] X. Li, R. Johnson, B. Weinstein, E. Wilder, E. Smith, G. B. Kasting, *Chem. Eng. Sci.* **2015**, *138*, 164.
- [10] Q. Sun, E. P. J. Parrott, Y. He, E. Pickwell-MacPherson, *J. Biophotonics* **2018**, *11*, e201700111.
- [11] J. Wang, Q. Sun, R. I. Stantchev, T.-W. Chiu, A. T. Ahuja, E. Pickwell-MacPherson, *Biomed. Opt. Express* **2019**, *10*, 3584.
- [12] H. Fujiwara, *Spectroscopic Ellipsometry Principles and Applications*, John Wiley & Sons, Chichester **2007**.
- [13] X. Chen, E. P. J. Parrott, Z. Huang, H. Chan, E. Pickwell-MacPherson, *Photonics Res.* **2018**, *6*, 768.
- [14] D. Grischkowsky, S. Keiding, M. van Exter, C. Fattinger, *J. Opt. Soc. Am. B* **1990**, *7*, 2006.
- [15] X. Chen, K. Li, R. Zhang, S. K. Gupta, A. K. Srivastava, E. Pickwell-MacPherson, *Adv. Opt. Mater.* **2019**, *7*, 1901321.
- [16] E. Pickwell, B. E. Cole, A. J. Fitzgerald, V. P. Wallace, M. Pepper, *Appl. Phys. Lett.* **2004**, *84*, 2190.
- [17] E. Pickwell, B. E. Cole, A. J. Fitzgerald, M. Pepper, V. P. Wallace, *Phys. Med. Biol.* **2004**, *49*, 1595.
- [18] A. K. Dąbrowska, C. Adlhart, F. Spano, G.-M. Rotaru, S. Derler, L. Zhai, N. D. Spencer, R. M. Rossi, *Biointerphases* **2016**, *11*, 031015.
- [19] M. Egawa, T. Hirao, M. Takahashi, *Acta Derm. Venereol.* **2007**, *87*, 4.
- [20] V. Conti Nibali, M. Havenith, *J. Am. Chem. Soc.* **2014**, *136*, 12800.
- [21] K. Tanaka, T. Arikawa, H. Yada, M. Nagai, *Optical Terahertz Science and Technology*, Optical Society of America, Washington, DC **2007**, p. MB1.
- [22] M. U. Heyden, G. Schwaab, E. Bründermann, X. Yu, D. M. Leitner, M. Havenith, *Proc. Natl. Acad. Sci.* **2006**, *103*, 12301.
- [23] S. Ebbinghaus, J. K. Seung, M. Heyden, X. Yu, U. Heugen, M. Gruebele, D. M. Leitner, M. Havenith, *Proc. Natl. Acad. Sci.* **2007**, *104*, 20749.
- [24] M. Hishida, K. Tanaka, *Phys. Rev. Lett.* **2011**, *106*, 158102.
- [25] C. S. Choe, J. Lademann, M. E. Darvin, *Analyst* **2016**, *141*, 6329.
- [26] G. K. Menon, G. W. Cleary, M. E. Lane, *Int. J. Pharm.* **2012**, *435*, 3.
- [27] C. R. Harding, *Dermatol. Ther.* **2004**, *17*, 6.
- [28] S. Verdier-Sévrain, F. Bonté, *J. Cosmet. Dermatol.* **2007**, *6*, 75.
- [29] J. Fowler, *Pract. Dermatology* **2012**, *9*, 36.
- [30] J. van Smeden, M. Janssens, G. S. Gooris, J. A. Bouwstra, *Biochim. Biophys. Acta Mol. Cell Biol. Lipids* **2014**, *1841*, 295.
- [31] Y. He, K. Liu, C. Au, Q. Sun, E. P. J. Parrott, E. Pickwell-MacPherson, *Phys. Med. Biol.* **2017**, *62*, 8882.
- [32] D. K. Hale, *J. Mater. Sci.* **1976**, *11*, 2105.
- [33] M. Scheller, C. Jördens, M. Koch, *Opt. Express* **2010**, *18*, 10137.
- [34] M. Scheller, C. Jansen, M. Koch, *Recent Optical and Photonic Technologies*, IntechOpen, London **2010**, pp. 231–250.
- [35] J. Clegg, M. P. Robinson, *Phys. Med. Biol.* **2012**, *57*, 6227.
- [36] K. Li, X. Chen, S. Shen, R. Zhang, E. Pickwell-MacPherson, *IEEE Trans. Terahertz Sci. Technol.* **2019**, *9*, 675.
- [37] X. Chen, Q. Sun, R. I. Stantchev, E. Pickwell-MacPherson, *APL Photonics* **2020**, *5*, 056104.
- [38] C. Rønne, L. Thrane, P. O. Åstrand, A. Wallqvist, K. V. Mikkelsen, S. R. Keiding, *J. Chem. Phys.* **1997**, *107*, 5319.
- [39] B. Scherger, M. Scheller, N. Vieweg, S. T. Cundiff, M. Koch, *Opt. Express* **2011**, *19*, 24884.
- [40] B. E. Cole, R. M. Woodward, D. A. Crawley, V. P. Wallace, D. D. Arnone, M. Pepper, *Commercial and Biomedical Applications of Ultrashort Pulse Lasers; Laser Plasma Generation and Diagnostics*, Vol. 4276, International Society for Optics and Photonics, Bellingham, WA **2001**, pp. 1–10.
- [41] C. S. King, S. P. Barton, S. Nicholls, R. Marks, *Br. J. Dermatol.* **1979**, *100*, 165.
- [42] A. V. Rawlings, P. J. Matts, *J. Invest. Dermatol.* **2005**, *124*, 1099.
- [43] C. S. Choe, J. Schleusener, J. Lademann, M. E. Darvin, *J. Dermatol. Sci.* **2017**, *87*, 183.
- [44] J. M. Crowther, A. Sieg, P. Blenkiron, C. Marcott, P. J. Matts, J. R. Kaczvinsky, A. V. Rawlings, *Br. J. Dermatol.* **2008**, *159*, 567.
- [45] R. R. Warner, K. J. Stone, Y. L. Boissy, *J. Invest. Dermatol.* **2003**, *120*, 275.
- [46] M. O. Visscher, G. T. Tolia, R. R. Wickett, S. B. Hoath, *J. Cosmet. Sci.* **2003**, *54*, 289.